THE ASTROPHYSICAL JOURNAL, 564:896–908, 2002 January 10

EXPERIMENTS TO PRODUCE A HYDRODYNAMICALLY UNSTABLE, SPHERICALLY DIVERGING SYSTEM OF RELEVANCE TO INSTABILITIES IN SUPERNOVAE

R. P. DRAKE,[1] H. F. ROBEY,[2] O. A. HURRICANE,[2] Y. ZHANG,[3] B. A. REMINGTON,[2] J. KNAUER,[4] J. GLIMM,[3] D. ARNETT,[5] J. O. KANE,[2] K. S. BUDIL,[2] AND J. GROVE[6]

Received 2000 June 5; accepted 2001 September 5

ABSTRACT

Results of the first spherically diverging, hydrodynamically unstable laboratory experiments of relevance to supernovae (SNe) are reported. The experiments are accomplished by using laser radiation to explode a hemispherical capsule, having a perturbed outer surface, which is embedded within a volume of low-density foam. The evolution of the experiment, like that of a supernova, is well described by the Euler equations. We have compared the experimental results to those of two-dimensional simulations using both a radiation-hydrodynamics code and a pure hydrodynamics code with front tracking.

Subject headings: hydrodynamics — methods: laboratory — supernovae: general

1. INTRODUCTION

While it has long been known that exploding stars are hydrodynamically unstable, the active exploration of the related effects has been relatively recent. This is a natural evolution following the development of computers and models that are now capable of treating such systems (Hachisu et al. 1991; Herant & Benz 1991; Muller, Fryxell, & Arnett 1991; Chevalier, Blondin, & Emmering 1992). The particular case of SN 1987A, however, has added great impetus to these efforts. In this case, a one-dimensional, spherically symmetric explosion model could explain neither the observed light curve nor the direct observation of X-ray emission from ^{56}Co (Arnett et al. 1989; Chevalier 1992). Some source of very active "mixing" of the inner and outer layers was required. It soon became clear, however, that computer models exploring the effects of two-dimensional hydrodynamic mixing, which could be investigated on the scale of the entire star, could not explain the observed velocities of the high-Z elements (McCray 1993). Three-dimensional effects increase the mixing, but appear to remain insufficient to explain the actual data (Herant & Benz 1992; Kane et al. 2000). SN 1987A remains an enigma.

A number of possible explanations for these discrepancies are under active exploration. It could be that structure within the star, prior to the explosion, acts to enhance the outward penetration of the inner layers (Bazan & Arnett 1994, 1998; Arnett 2000). It could be that the explosion itself is inherently asymmetric (Khokhlov et al. 1999). It could be that neutrino-driven overturn during the first second of the explosion provides the additional impetus needed to produce the large observed velocities (Kifonidis et al. 2000). Or it could be that the existing computer models do not correctly calculate the hydrodynamic behavior. We discuss this point next.

It may seem unnecessary to test the computer models, from the point of view that "we understand hydrodynamics." However, it would be more accurate to say that we understand the equations that apply to hydrodynamics. It is less clear how well we understand how to numerically model the very nonlinear evolution of hydrodynamic systems. Like a series solution to a differential equation, a computer simulation is only an approximation to the actual solution of the physical equations being solved. Unlike a series solution, it is very difficult to judge the error involved in the approximate computational solution. Direct comparisons of simulation results with analytic solutions or with data are the only real measures of quality for a simulation. Of course, comparisons with analytic solutions are only possible for the simplest problems, so we have taken the second approach. The problem of judging the quality of a simulation is compounded in curved geometries, where one may encounter problems created by vanishing metrics even if one were using a hypothetically "perfect" numerical method on the system of physics equations involved. In addition, it remains unclear, from a fundamental hydrodynamic point of view, whether fine structures in an evolving turbulent system can significantly affect the large-scale evolution of the system, a process described in that literature as "stochastic backscatter" (Leith 1990; Piomelli et al. 1991). In all the codes now used for astrophysical modeling, this process is precluded by the numerical dissipation present in the codes. If it were important, this would lead to differences between simulations and well-formulated test experiments.

One sees significant differences among approaches to numerical hydrodynamics, as well. Specifically, while various codes generally agree on the large-scale morphology of developing instabilities, they disagree quantitatively regarding the asymptotic velocities of unstable features (Glimm et al. 2001). This could impact the extent of the unstable "mix layer" that develops in astrophysical systems. In addition, at any spatial scale below one-tenth of an initial perturbation wavelength, different codes or models within them produce very different fine-scale structures (Kane et al. 1998). This too could have important consequences, such as determining whether or not such structures might produce hydrodynamic "bullets"

[1] Atmospheric, Oceanic, and Space Sciences, University of Michigan, 2455 Hayward Street, Ann Arbor, MI 48109; rpdrake@umich.edu.

[2] Lawrence Livermore National Laboratory, 7500 East Avenue, Livermore, CA 94550; robey1@llnl.gov, hurricane1@llnl.gov, remington2@llnl.gov, jave@llnl.gov, budil1@llnl.gov.

[3] State University of New York at Stony Brook, Stony Brook, NY 11794; yzhang@ams.sunysb.edu, glimm@ams.sunysb.edu.

[4] Laboratory for Laser Energetics, University of Rochester, 250 East River Road, Rochester, NY 14623; jkna@sequoia.lle.rochester.edu.

[5] Steward Observatory, University of Arizona, Tucson, AZ 85721; darnett@as.arizona.edu.

[6] Los Alamos National Laboratory, Los Alamos, NM 87545; jgrove@lanl.gov.

(MacLow 1995; Stone, Xu, & Mundy 1995). In view of all of the above, we believe that experimental tests of the codes that model astrophysical (and other) hydrodynamics are crucial.

The need to assure that these models do correctly calculate such behavior has been the focus of a recent effort to produce scaled conditions in laboratory experiments (Remington et al. 1997, 1999, 2000; Drake 1999; Kane et al. 1999). The present experiment is part of that ongoing effort, which includes the work just cited and other work now underway or being planned. The goal of the community doing this work is to observe the hydrodynamic mechanisms that are important in the evolution of core-collapse supernovae and remnants, in order to test the simulation codes and to provide direct evidence of how these mechanisms operate. The connection to the global scale cannot be made by experiments; it will have to be done in simulations. The prior experiments have all been performed in planar geometry, which has the advantage of permitting the maximum possible nonlinear development of hydrodynamic instabilities. The disadvantage of planar experiments is that they do not test the ability of the models to calculate the evolution of instabilities in a spherically divergent geometry. This is the case of importance to the explosion phase of supernovae (SNe), and it does introduce some alterations in the details of the simulations. In the present paper, we report the results of the first experiments to produce a spherically expanding, hydrodynamically unstable system whose scaled parameters make it a reasonable test case for the computational astrophysical models. We considered this experiment worthwhile, as a direct experimental test in a spherically expanding system, even though we did not think it probable that the computational models would prove to be substantially in error.

To place this work most clearly in context, it is worth mentioning that a number of previous experiments in spherical geometry, with some degree of astrophysical relevance, have been undertaken. Most of them involve the dynamics of isolated blast waves (see, e.g., Grun et al. 1991), and none of them are aimed at the dynamics that occurs during SN explosions. Most of these experiments are reviewed by Drake (1999). Two others worth mentioning are by Ripin et al. (1987, 1990, 1993) and by Dimonte & Wiley (1991); this work investigated the instability of magnetized blast waves in a regime where large-gryoradius effects mattered.

In the following, we first discuss the problem of scaling from the laboratory to the SN; then we discuss the methods by which the experiments were conducted. Section 4 presents the experimental results. Turning to simulations, § 5 reports our simulations of this system using a radiation-hydrodynamics code, and § 6 describes how one can use a purely hydrodynamic code to model the system and shows results from one such effort. A concluding section then follows.

2. SCALING ISSUES

Conner & Taylor (1977), and more recently Ryutov et al. (1999), have presented general scaling relations that govern the validity of experiments intended to replicate the hydrodynamic phenomena occurring in astrophysical systems. In this section, we apply those scaling relations to the problem of the effect of spherical divergence on instability evolution in the explosion phase of SNe. Specifically, the emphasis is placed on studying the instability evolution at the He/H interface in SNe with experiments conducted on the Omega Laser (Boehly et al. 1995, 1997; Soures et al. 1996; Bradley et al. 1998) at the Laboratory for Laser Energetics (LLE), University of Rochester. The more dense He layer is simulated with a Ge-doped CH hemispherical capsule ($\rho = 1.37$ g cm^{-3}) of finite thickness, and the surrounding H layer is simulated with a low-density ($\rho = 0.1$ g cm^{-3}) carbon foam. In the Omega experiment, a strong shock, launched by laser ablation pressure, is driven through this interface. Figure 1 shows the resulting density and pressure fields near the interface of interest for both the SN at $t = 2000$ s and the corresponding scaled Omega experiment at $t = 20$ ns. In both cases, the outward-propagating shock is off to the right of the figure. Figure 1*a* is taken from a one-dimensional simulation using the astrophysical code PROMETHEUS (Muller et al. 1991), and Figure 1*b* is taken from a one-dimensional HYADES (Larsen & Lane 1994) simulation of the scaled experiment on the Omega laser. The geometrical similarity, near the interface, between the two vastly disparate scales is readily apparent. This geometrical similarity is only local, however, and farther from the interface, the two systems will differ. Outside of the interface, for example, the radial density distribution in the star decreases rapidly, while the density in the experiment remains constant.

The deceleration of the interface is similar but not identical in the two cases, in part as a result of these geometrical differences. Figure 2 shows the velocity of the interface, again from the simulations, in the laboratory and in SN 1987A. One sees that the shape of these curves is similar, but that the interface decelerates more quickly in the experi-

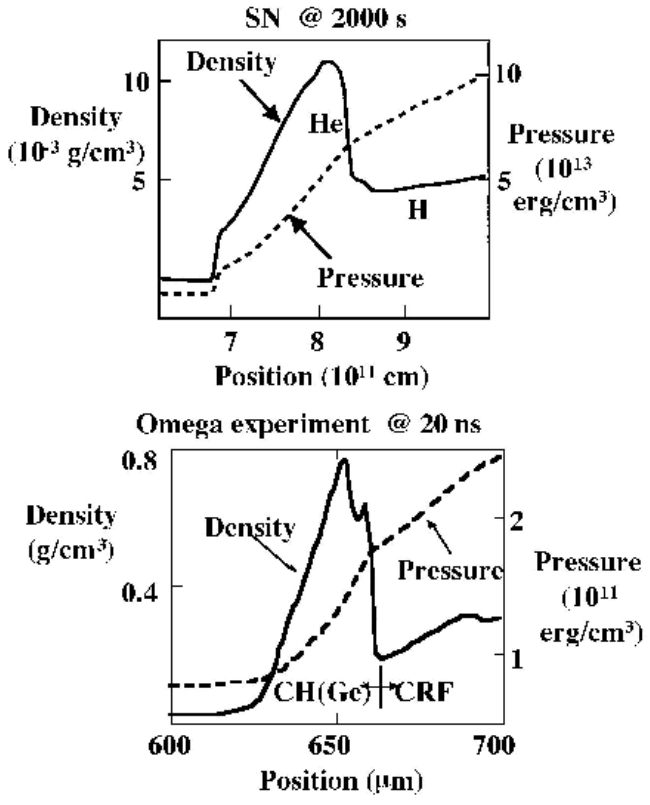

FIG. 1.—(*a*) Pressure and density from one-dimensional PROMETHEUS simulation of He/H interface of SN. (*b*) Pressure and density from one-dimensional HYADES simulation of CH(Ge)/CRF interface of a scaled Omega experiment.

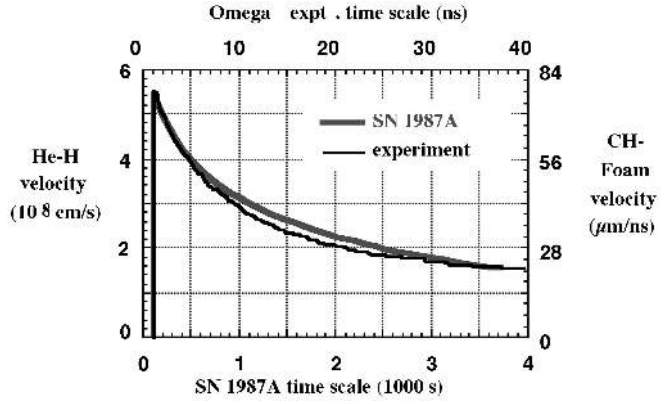

FIG. 2.—Time dependence of the velocity of the interface between high and low density is shown. The bottom and left scales apply to SN 1987A. The top and right scales apply to the laboratory experiment.

ment. This is very likely a consequence of the difference in the density profile in the low-density region. The consequences are discussed further below.

Table 1 shows a comparison between the physical scales involved in the SN and the laboratory experiment. The characteristic length scale differs by 14 orders of magnitude, and the pressure, density, temperature, and ionization state show considerable differences as well. Table 2 gives several of the important derived parameters that quantify the degree of scaled similarity and the applicability of the Euler equations to these two problems. The first parameter, $v/(p/\rho)^{1/2}$, which has the form of a Mach number, establishes the degree to which the two systems will exhibit similar behavior. This parameter is nearly equal for the two systems. If the boundary conditions were also identical, then they would indeed evolve identically. In fact, the geometric differences just identified, and the consequent differences in the acceleration history of the interface, imply that the evolution will not be identical. Nonetheless, the systems are sufficiently similar that the laboratory system is a relevant test of many aspects of the effects of spherical divergence on instability evolution in SN. This assumes that the Euler equations apply, which is discussed next.

TABLE 1

FUNDAMENTAL HYDRODYNAMIC PARAMETERS

Parameter	Supernova	Omega Experiment
Length scale (cm)	9×10^{10}	0.0023
Velocity (km s^{-1})	2000	14
Density (g cm^{-3})	0.0075	0.4
Pressure (dyne cm^{-2})	3.5×10^{13}	1.5×10^{11}
Temperature (eV)	900	2
Z_i	2.0	0.5
A	4.0	8.7
Density of nuclei (cm^{-3})	1.1×10^{21}	2.8×10^{22}

TABLE 2

DERIVED PARAMETERS

Derived Parameter	Supernova	Omega Experiment
$v/(p/\rho)^{1/2}$	2.2	2.3
Collisional mfp (cm)	3.6×10^{-3}	4.0×10^{-9}
Kinematic viscosity (cm^2 s^{-1})	7.0×10^{7}	0.02
Reynolds number	1.9×10^{11}	1.4×10^{5}
Thermal diffusivity (cm^2 s^{-1})	1.2×10^{6}	0.55
Peclet number	1.1×10^{13}	5.9×10^{3}
Radiation mfp (cm)	6.8×10^{2}	2.0×10^{-6}
Radiation Peclet number	1.6×10^{16}	1.6×10^{10}

The applicability of the Euler equations is quantified by demonstrating that dissipative processes such as viscosity, thermal conductivity, and radiative transport are small in comparison with the inertial terms in the equations of motion (Table 2). These processes are quantified by the appropriate nondimensional parameters: the Reynolds number, Peclet number, and radiation Peclet number. All these were discussed by Ryutov et al. (1999). In that work, the viscosity and thermal conductivity were estimated using simple analytical formulae (Braginski 1965) applicable to the high-temperature, low-density plasmas characteristic of SNe. For the laboratory plasma, however, the temperature can be much lower and the density considerably higher than that in the SN (see Table 1). In this case, the plasma ions are no longer necessarily weakly coupled, and the kinetic theory approach of Braginski is not always appropriate. For such dense plasma conditions, we use an improved model for the thermal conductivity (Lee & More 1984), which is applicable over a broad range of parameter space.

For dense plasma conditions and for conditions where mixing between two ionic species is involved, we also use an improved viscosity model (Clerouin, Cherfi, & Zerah 1998), which is applicable over a wider range of temperatures and densities than the Braginski model. For this model, the kinematic viscosity is given by

$$v(\mathrm{cm}^2\ \mathrm{s}^{-1}) = 6.55 \times 10^{-10} Z_{\mathrm{eff}}\, m_i^{1/2}\, n_i^{5/6} \times \begin{cases} 1.1\Gamma_{\mathrm{eff}}^{-1.895} & \Gamma_{\mathrm{eff}} < 2 \\ \lambda I_1 + \dfrac{(1+\lambda I_2)}{\lambda I_3} & 2 < \Gamma_{\mathrm{eff}} < 160\ , \end{cases} \quad (1)$$

where the parameter λ and fits to the integrals I are given by

$$\lambda = \frac{4\pi}{3}(3\Gamma_{\mathrm{eff}})^{3/2}\ ,$$

$$I_1 = (180\pi^{3/2}\Gamma_{\mathrm{eff}})^{-1}\ ,$$

$$I_2 = \frac{1}{60\pi^2}(0.49 - 2.23\Gamma_{\mathrm{eff}}^{-1/3})\ ,$$

$$I_3 = \frac{1}{10\pi^{3/2}}(2.41\Gamma_{\mathrm{eff}}^{1/9})\ . \quad (2)$$

Here $Z_{\mathrm{eff}} = x_1 Z_1 + x_2 Z_2$ is the number-density–weighted average charge for a binary ionic mixture of two species with fractional number densities x_1 and x_2. The effective plasma coupling parameter for this mixture is

$$\Gamma_{\mathrm{eff}} = \frac{e^2 Z_{\mathrm{eff}}^{1/3}\overline{Z^{5/3}}}{a k_{\mathrm{B}} T}\ , \quad \overline{Z^{5/3}} = x_1 Z_1^{5/3} + x_2 Z_2^{5/3}\ , \quad (3)$$

where a is the mean ionic radius, and k_{B} is the Boltzmann constant. For plasma conditions of high temperature and low density, this model gives results in good agreement with the model of Braginski (1965).

One sees in Table 2 that the Reynolds number, the Peclet number, and the radiation Peclet number are all large for the SN as well as for the Omega experiment. This indicates that for the large-scale features of interest (shock and inter-

face positions, growth of perturbations of wavelength comparable to the system size, etc.), the Euler equations apply, and that viscous, thermal, and radiation effects can be neglected. At a sufficiently small spatial scale, which will be a small fraction of the system size, these effects may no longer be negligible. On that scale, as previously discussed (Ryutov et al. 1999), dissipation will affect the structure of the resulting turbulence.

3. EXPERIMENTAL SETUP

Figure 3 shows a schematic of the Omega experiment. In order to investigate the instability at an interface where the density decreases, targets were prepared that consisted of a hemispherical shell of CH(3% Ge) with a density $\rho = 1.37$ g cm^{-3} surrounded by a volume of lower density foam. The capsule inside diameter (ID) was nominally 440 μm, and the shell thickness, Δr, was 96–109 μm in various experiments. (The later experiments used thicker shells, with the aim of delaying the breakup of the capsule. This made very little qualitative difference in the observed dynamics.) The capsule was embedded within a cylinder of carbonized resorcinol formaldehyde (CRF), a porous foam with density $\rho = 0.1$ g cm^{-3}. (In one case shown below, the foam density was 0.05 g cm^{-3}.) The CRF cylinder measured 1500 μm in diameter by 1500 μm in length.

An initial perturbation was imposed on the outer surface of the CH(Ge) capsule. The perturbation, produced by laser ablation, has a wavelength $\lambda = 70$ μm and a peak-to-valley amplitude of $a_{p\text{-}v} = 10$ μm. Two perturbation geometries were used in the experiments. Most of the experiments employed a two-dimensional perturbation geometry, in which the ripples form parallel grooves in the outer CH(Ge) capsule that are oriented parallel to the diagnostic line of sight. This provides a clear, well-defined side-on view of the ripple amplitude for back-illuminated radiography. The disadvantage of this geometry is that it is fully three-dimensional, and is thus difficult to simulate numerically. The second geometry is an azimuthal or "bulls-eye" ripple pattern with the same wavelength and amplitude. This geometry is cylindrically symmetric and therefore conforms more closely to that used in two-dimensional numerical simulations of the experiment. It has the disadvantage, however, of not having a clear side-on diagnostic line of sight. Results from both perturbation geometries will be shown and discussed.

The target is driven by six beams of the Omega laser with a nominal measured energy of 420 J beam^{-1} at a laser wavelength of 0.351 μm. The six beams, each of which form an angle of 23°.2 from the target normal in a hexagonal pattern, are overlapped at the target center. Each beam has a super-Gaussian spatial profile. The combined spatial profile of the drive beams is well represented by the intensity profile $I/I_0 = \exp[-(r/412\ \mu\text{m})]^{4.7}$, with $I_0 = 5.4 \times 10^{14}$ W cm^{-2}. With this profile, the average intensity over a 440 μm diameter spot is 5.3×10^{14} W cm^{-2}. The temporal pulse duration is 1 ns. Since the laser beam spot size is greater than the ID of the spherical capsule, a gold shield 25 μm thick by 2.5 mm diameter was used to delay the propagation of the resulting planar shock around the sides of the capsule. This target structure proved to be successful in generating a very nearly spherical explosion of the capsule.

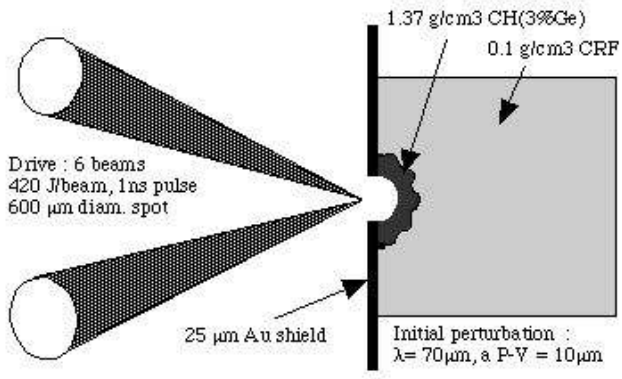

FIG. 3.—Schematic of experiment

The evolution of the instability at the capsule outer surface was diagnosed with 4.3 keV X-rays generated by directing an additional eight Omega beams onto a 12 μm thick Sc backlighter foil located 4 mm from the center of the target. These beams, driven by a separate oscillator, were delayed in time relative to the drive beams by up to 40 ns to observe the instability evolution at late times. Differential absorption of the backlighter X-rays, which were imaged with a gated framing camera (Budil et al. 1996), produced contrast in the X-ray images.

4. EXPERIMENTAL RESULTS

Figure 4 shows three experimental radiographs of the instability evolution. In Figure 4*a*, an unperturbed capsule is shown at $t = 13.6$ μs as a reference case. Several features can be observed from this null experiment. The capsule shell is seen to remain intact, with no evidence of instability growth. By comparison with the initial capsule position, the shell radius has expanded to $R/R_0 = 2.7$, and the capsule thickness has decreased to approximately half of its initial value. The expanded capsule shape is seen to be very nearly spherical. The shock is clearly seen in the image just outside of the expanding shell. Figure 4*b* shows the corresponding image at the same time, $t = 13.6$ μs, for a capsule with a $\lambda = 70$ μm and nominal $a_{p\text{-}v} = 10$ μm perturbation. Again, the radial divergence factor is 2.7. The wavelength of the perturbation is seen to have grown by a similar factor. These two features, the capsule thinning and the increase in perturbation wavelength, are the two essential features that differentiate the instability evolution in spherically divergent geometry from what is observed in the much more extensively studied case of planar geometry.

Figure 4*c* shows the continued evolution of the instability at $t = 26$ ns. The overall capsule shape remains reasonably spherical, with a spherical divergence factor of 3.4. From Figures 4*b* and 4*c*, the shock position, which is very close to that of the interface, is seen to correspond almost exactly to that of a spherically expanding Taylor-Sedov blast wave with $R_{26}/R_{13} = (t_{26}/t_{13})^{2/5}$, where the subscripts indicate the time in ns. The amplitude of the perturbation is difficult to measure in Figure 4*c*, since the capsule has completely broken up, with all of the more dense capsule material appearing in the spikes that lie very close to the shock front.

There are three notable differences between the experimental system and an actual SN. First, the capsule shell is of finite radial extent. By contrast, the layers of He and H in the SN can be approximated as semi-infinite fluids. Second, the shock in the scaled Omega experiment is propagating into material of constant density, whereas in the SN the

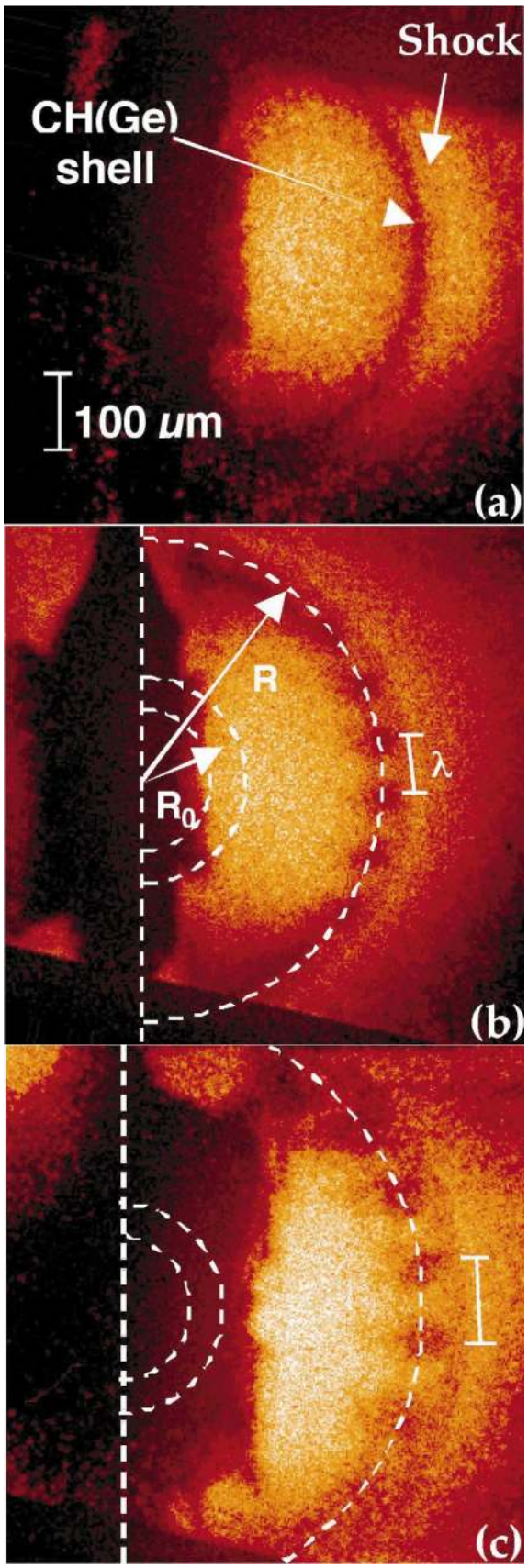

FIG. 4.—Radiograph of (*a*) an unperturbed target at $t = 13.6$ ns: experiment 17,517 with ID = 424 μm, $\Delta r = 97$ μm; (*b*) a perturbed capsule at $t = 13.6$ ns: experiment 17,518 with ID = 435 μm, $\Delta r = 97$ μm; and (*c*) a perturbed capsule at $t = 26$ ns: experiment 17,524 with ID = 438 μm, $\Delta r = 96$ μm.

density falls off radially fast enough that the shock will continue to accelerate away from the interface. Third, as a consequence of the radial density distribution, the time dependence of the interface deceleration is not identical in the SN and the laboratory. In both the laboratory experiment and the SN, the unstable interface is first perturbed by a shock and then decelerates. In the case of the SN, the interface decelerates as the blast wave accelerates outward and pulls away from the interface, as illustrated for example in Kane et al. (1997). In the present experiment, the shock wave moves out into constant-density matter and is observed to decelerate like a Sedov-Taylor blast wave. The interface decelerates somewhat more rapidly than the shock wave, a result of the accumulation of matter between the interface and the shock. As discussed above, these differences imply that the scaled growth of the unstable structures will not be identical. For example, the Rayleigh-Taylor (RT) growth in the laboratory experiment may be impeded because of the proximity of the RT spikes to the shock, which acts roughly as a rigid boundary. This proximity effect is not likely to occur in a star, because of the continued acceleration of the shock. Nonetheless, the similarity in scaled parameters makes the experimental problem a reasonable test case for studying many aspects of instability development in divergent geometry.

In order to determine how to interpret the radiographs, we modeled the X-ray absorption of capsules with modulated surfaces. We concluded that we can infer the modulation amplitude from the images during the period until the capsule breaks up. After that, we cannot uniquely interpret the image but can only check consistency with simulations. Figure 5 shows an image, with higher magnification than that of the data shown in Figure 4, of a modulated capsule at 13 ns. We conclude from analyzing this image that the perturbation amplitude is 60 ± 10 μm, which is 6.5 ± 1.1 times the actual initial amplitude of 9.2 μm. (The modulation inferred from Fig. 4*b* is the same to within the uncertainties, and data at $t = 18$ ns showed a modulation of 88 ± 22 μm.) One can also see other features in Figure 5. The forward shock is evident, and appears to have been perturbed by the spikes. The dark region corresponding to each spike extends only a finite distance to the left, because the spikes were initially ablated from a square patch on the capsule surface. The finite size of the backlighter X-ray source produces a variation in the transmitted X-ray intensity through the unshocked foam.

The numerical simulations of this experiment were performed with two-dimensional codes, as described in the next two sections. In a two-dimensional simulation, it is not possible to correctly model the type of perturbation that was used in the experiments, since it is fully three-dimensional. In order to attempt a better comparison with the numerical simulations, a different type of initial perturbation geometry was used in some experiments. The perturbation was identical in both wavelength and amplitude to that imposed on the targets previously discussed, but the geometry is now azimuthally symmetric about the target central axis. Three periods of this perturbation (concentric rings) were imposed on the capsule outer diameter using laser ablation. A radiograph of the resulting instability structure is shown in Figure 6. The three cycles of the perturbation are clearly seen and can be compared directly with simulated radiographs from the numerical simulations. In working with the data, however, we found that the

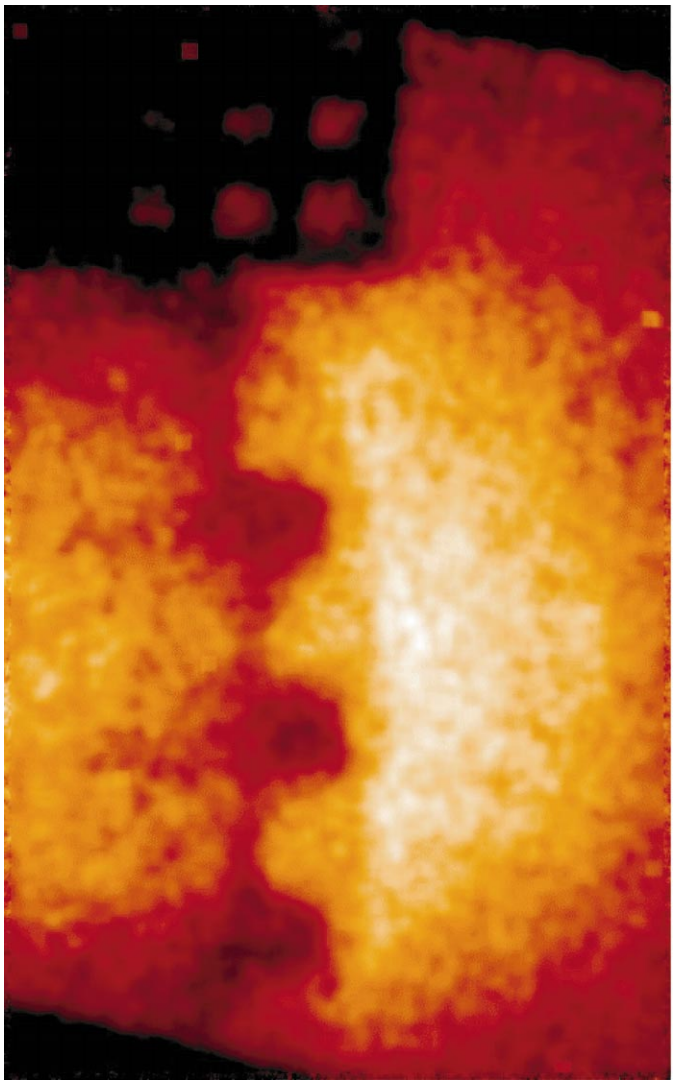

FIG. 5.—Higher magnification radiograph of perturbed capsule at $t = 13$ ns: experiment 20,620 with ID = 443 μm, $\Delta = 109$ μm. The dimensions of the wire grid are 62.5 μm from wire center to wire center.

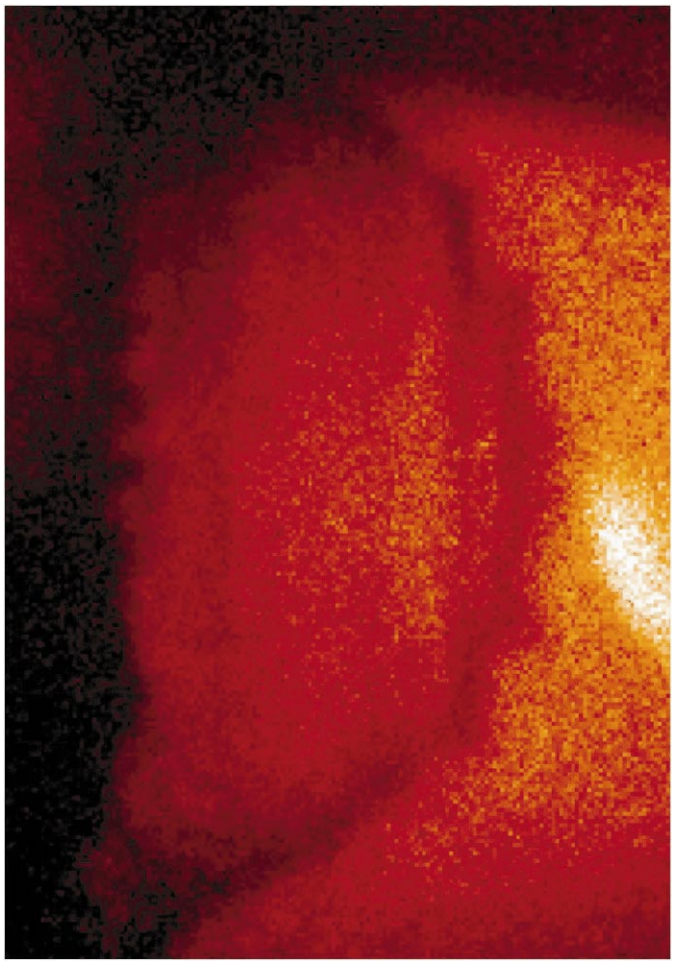

FIG. 6.—Radiograph of perturbed capsule with azimuthal perturbation geometry at $t = 13$ ns: experiment 19,714 with ID = 440 μm, $\Delta r = 109$ μm, and 50 mg cm^{-3} foam.

images of Figures 4 and 5 were more useful, since they allowed a better quantitative identification of the spike amplitudes. The experiment of Figure 6 is also one of several cases in which we used a lower foam density (0.05 g cm^{-3} rather that 0.1 g cm^{-3}), in order to see if this allowed significantly larger spike growth by allowing the forward shock to propagate further in front of the interface. This did not make any qualitative difference in the observed images.

5. COMPARISON WITH A RADIATION-HYDRODYNAMIC SIMULATION

The CALE (C-based Arbitrary Lagrangian-Eulerian) two-dimensional radiation hydrodynamics code (Barton 1985) has been used to explore the behavior of the target package of this experiment. The simulation uses a nonuniform grid of 150 × 120 zones in a cylindrical coordinate system (see Fig. 7), tabulated equations of state (EOS) for all of the component materials, and tabulated opacities. Laser energy (of intensity 5×10^{14} W cm^{-2}, in a 1 ns pulse) is deposited into the problem by ray-tracing 120 beamlets and depositing energy where the local plasma frequency (ω_{pe}) matches the laser frequency ($\omega = 8.57 \times 10^{14}$ s^{-1}). A Thomas-Fermi model is used to compute the ionization level of the material. The beamlets that compose the laser source fan out from a common focal point at an angle of 23°.2 measured from the symmetry axis. The focal point of the laser source is chosen so that the energy deposition pattern on the inner surface of the target matches the measured super-Gaussian profile (with spot size 824 μm) as closely as possible. Ultimately, this laser irradiation pattern deposits 58% of the laser energy onto the capsule inner surface with the remainder being deposited onto the Au radiation shield. In addition to the simple laser source model, a Lee-More electron conduction model (Lee & More 1984) and a flux-limited point-Jacobi, conjugate-gradient, thermal-radiation diffusion model are also implemented. Except for the symmetry axis, the boundaries are fixed, and the simulation is made large enough that the boundaries have no effect on the phenomena of interest. All the simulation results shown here are for a 109 μm thick capsule, whose surface is modulated by a 10 μm peak-to-valley, 70 μm wavelength sinusoid.

Early simulations exhibited a Courant-condition time-step problem as hot plasma ablated from the inner CH(Ge) capsule formed a jet which propagated over the center of convergence of the mesh. This problem was latter remedied by forcing the zones to the left of the capsule and shield to be Eulerian instead of ALE after an initial equipotential

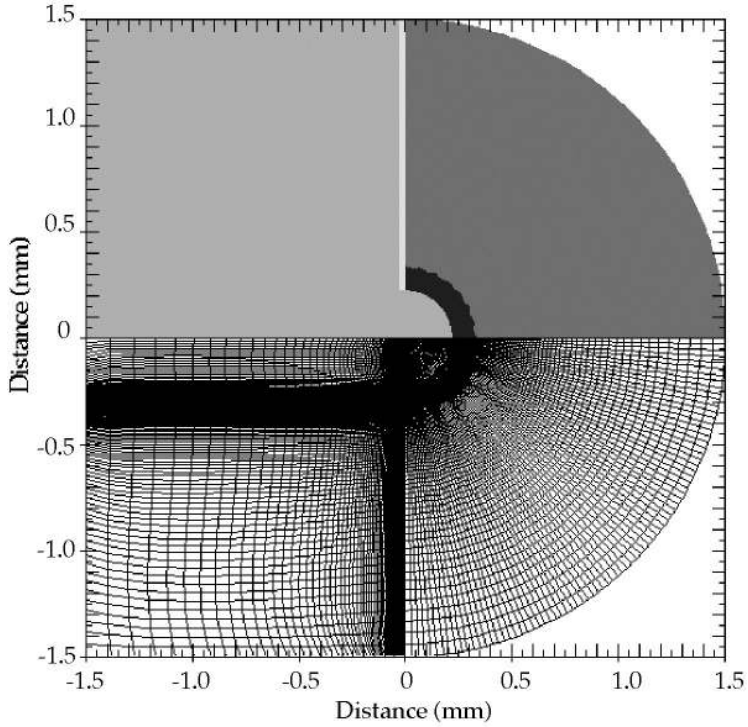

FIG. 7.—Material regions and initial mesh. The blue region is the CH(Ge) capsule of density $\rho = 1.37$ g cm^{-3}, the magenta region is the carbon resorcinol foam (CRF) of density $\rho = 0.05$ g cm^{-3}, the yellow region is the gold radiation shield of density $\rho = 19.3$ g cm^{-3}, and the cyan region is the vacuum region, which is treated as very low density air ($\rho = 1.23 \times 10^{-6}$ g cm^{-3}) with zero opacity. Imposed on the CH(Ge)-CRF boundary is a wavelength $\lambda = 70$ μm and peak-valley amplitude 10 μm perturbation. Reflected across the symmetry boundary, the mesh is shown. The zones are concentrated around regions that will later expand as energy is deposited into the problem. The spatial size of the figure corresponds to a 3000 μm square.

mesh relaxation in this region. As can be seen in Figure 8*b*, as early as 1 ns ablated plasma from the CH(Ge) capsule and CH coating on the Au shield has already reached the left simulation boundary, albeit with very little density (and with no subsequent effect on the phenomena of interest). By 1 ns, a $\sim 5 \times 10^{13}$ dyne cm^{-2} (50 Mbar) shock propagating outward is present in the CH(Ge) capsule. By carrying hot plasma toward the center of convergence of the capsule, the CH(Ge) jet has the beneficial effect of isotropizing the energy deposition on the back of the capsule through electron conduction and thermal reradiation effects. This behavior (see Figs. 8*a* and 8*b*) is like that of a radiation cavity, i.e., a hohlraum (Lindl 1998). The color bars shown in Figures 8 and 9 all correspond to a linear variation between the limits shown.

Figures 9 and 10 show simulation results from $t = 13$ and 26 ns, respectively. At 13 ns (Fig. 9) it is observed from the simulations that the transmitted shock has a slight ellipticity ($R_{\rm major}/R_{\rm minor} = 1.2$). The average interface position is 725 μm. Figure 9*a* shows material density with the color levels ranging from 0 to 0.5 g cm^{-3}. The thin black lines denote material boundaries. Figure 9*b* shows material pressure with the color levels ranging from 0 to 6.6×10^{11} dyne cm^{-2} (0.66 Mbar). At this time the capsule appears to remain intact, as can be seen by the density contrast across the material boundary between the CH(Ge) capsule and the foam. The radiation shield has expanded into the region left behind by the capsule. The Sedov-like transmitted shock wave is clearly visible in the figures. A transmission radiograph is shown in Figure 9*c*. Note that in the simulated radiograph, the perturbations create vertical streaks due to the azimuthal invariance of the two-dimensional simulation. The correspondence with the experimental radiograph of the azimuthally perturbed target as shown in Figure 6 is qualitatively quite good.

At 26 ns (Fig. 10), the simulations show that the ellipticity of the shock has decreased to 1.14. The forward shock is now at 1200 μm and the average position of the interface at 850 μm. In addition to the large growth seen in the simulations by 26 ns, the fingers also exhibit a significant counterclockwise curling, an effect that might be attributed to imprinting of the initial shock breaking out of the capsule in the forward direction (to the right in the figures) before breaking out at 90° with respect to the symmetry axis. Similar to Figure 9, Figure 10*a* shows the density, with the color levels ranging from 0 to 0.5 g cm^{-3}; Figure 10*b* shows the pressure, with the color levels ranging from 0 to 6×10^{11} dyne cm^{-2} (0.6 Mbar); and Figure 10*c* shows the simulated transmission radiograph. Examination of these figures show that there is very little, if any, pressure variation across the material boundary between the CH(Ge) and the foam. The fingers of the perturbations appear to contain small nodules of density, but lack any material connection to each other, suggesting that the capsule has broken up by this time, in agreement with the observations from experiment, as shown in Figure 4*c*.

While CALE qualitatively reproduced the experimental data, as we have discussed, this required that the model incorporate laser transport, laser absorption, electron heat conduction, and radiation. In using these data to test astrophysical models, it would be self-defeating to require that they include all the same features. This is because the effort to incorporate them is not justified by their purposes in astrophysics, and because any disagreements with the data

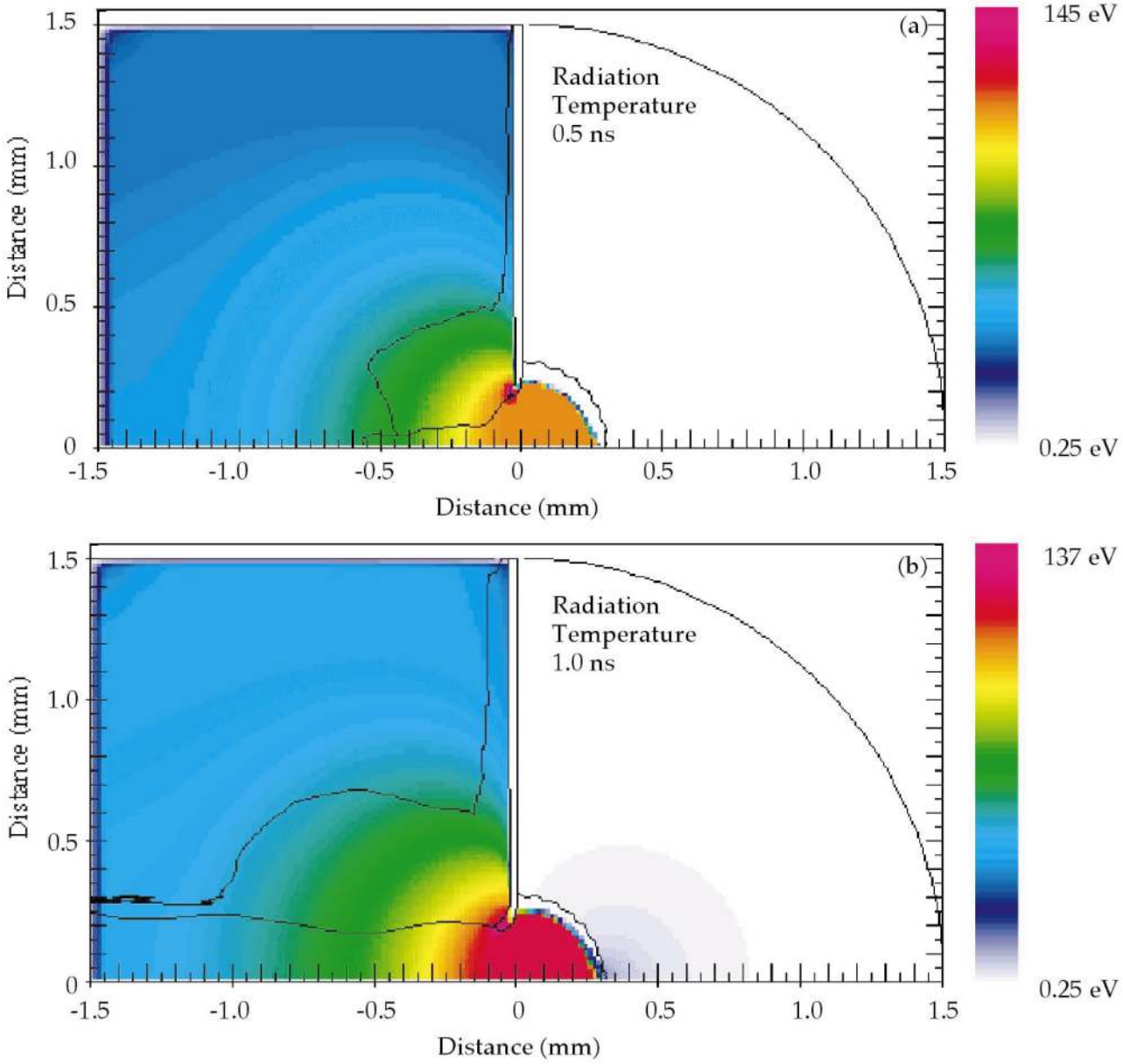

FIG. 8.—Radiation temperatures at (*a*) $t = 0.5$ ns and (*b*) $t = 1.0$ ns. The thin black lines denote material boundaries. In the regions in the vicinity of the inner radius of the capsule, the radiation pattern is extremely uniform in spite of the fact that the laser deposition is directional. The variation in temperature is linear over the range shown by the color bar.

might just as easily result from errors in these additional models as from problems with the hydrodynamics. To avoid these difficulties, we have adopted the following method, which has been successfully applied to other problems, as in Kane et al. (1997). We note that all of these other effects are only dominant during the first 1 ns of the simulation. After that time, during the ensuing 30 ns that are of interest, they do not significantly affect the flow evolution. The method is to transfer the profiles of the hydrodynamic parameters, at a time after which the evolution is purely hydrodynamic. It is also important that the hydrodynamic state of the system, at the time when the parameters are recorded, is simple enough that the transfer can be done accurately. In the present case, this must be before the shock reaches the perturbed interface. This led to us to transfer the parameters at a time of 2 ns. (This worked reasonably well, as is seen below. However, to completely assure that non-hydrodynamic effects are negligible, we would prefer to use a thicker capsule or make other equivalent changes in future experiments, so that the transfer of parameters could be done at 2.5–3 ns.) We can provide profiles of the hydrodynamic parameters, at 2 ns, to anyone who is interested in applying their simulation code to this system. The next section discusses one such exercise.

6. AN EXAMPLE OF A HYDRODYNAMIC SIMULATION

As an example of this procedure and its results, we have mapped the results from CALE into a purely hydrodynamic code named FronTier. FronTier is based on a front-tracking method in which a lower dimensional moving grid is fitted to and follows the dynamical evolution of distinguished waves in a fluid flow. In this simulation, we are interested in the evolution of a material interface (contact front) separating fluids of distinct densities. The ideas of

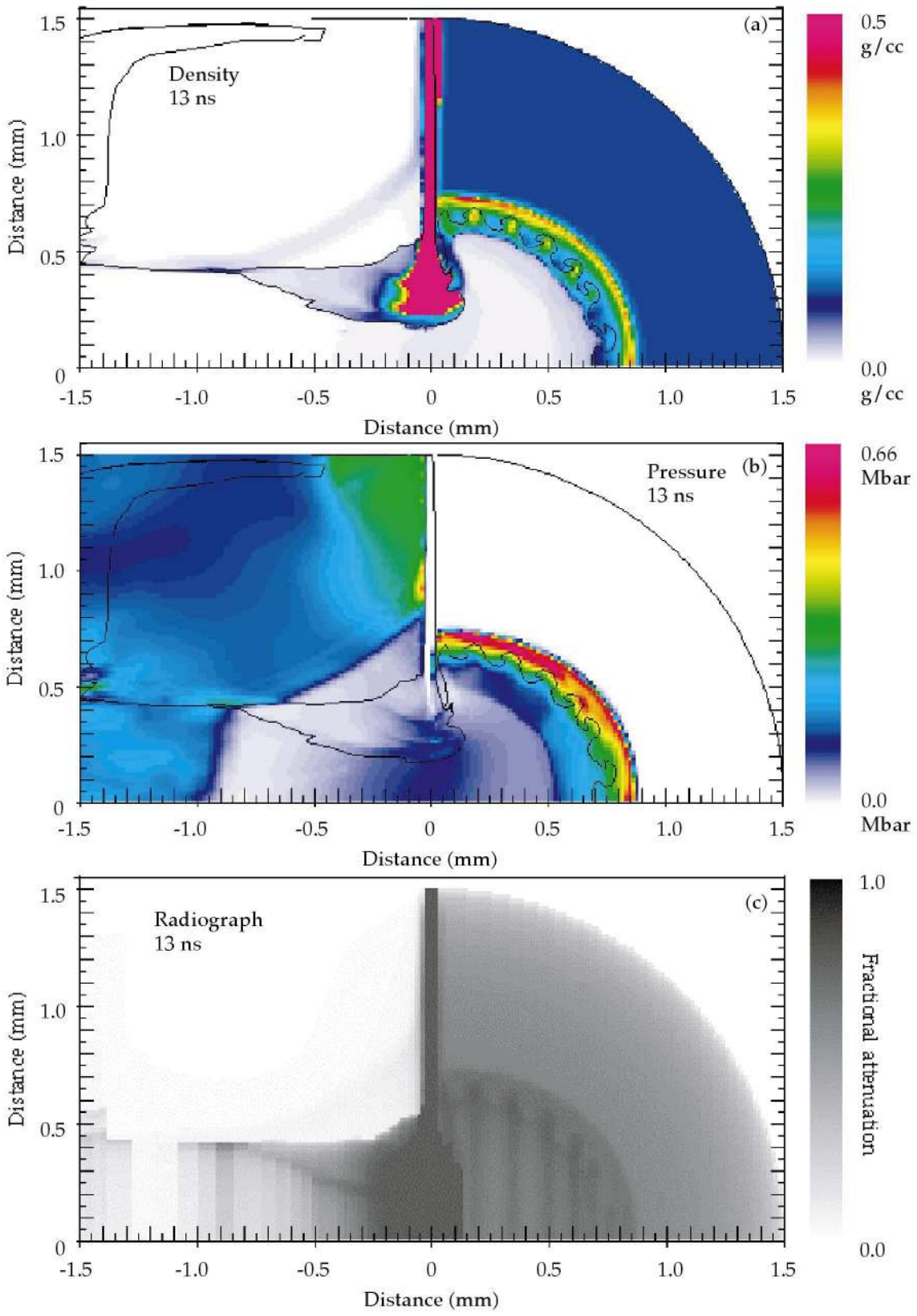

FIG. 9.—Plots of (*a*) the material density, (*b*) the pressure, and (*c*) the transmission radiograph at $t = 13$ ns. In (*a*) the color levels range from 0 to 0.5 g cm^{-3}. In (*b*) the color levels range from 0 to 0.66 Mbar (6.6×10^{11} dyne cm^{-3}). Material boundaries are traced with thin black lines.

front tracking can be described briefly as follows. We project the front dynamics into normal and tangential directions, which are thus split into two one-dimensional problems, accordingly. The problem in the normal direction is a nonlocal Riemann problem. After updating the states on each side of the discontinuity, we move the front point by the computed wave speed. Next, we solve the problem in the tangential direction. Since this is a smooth problem, we

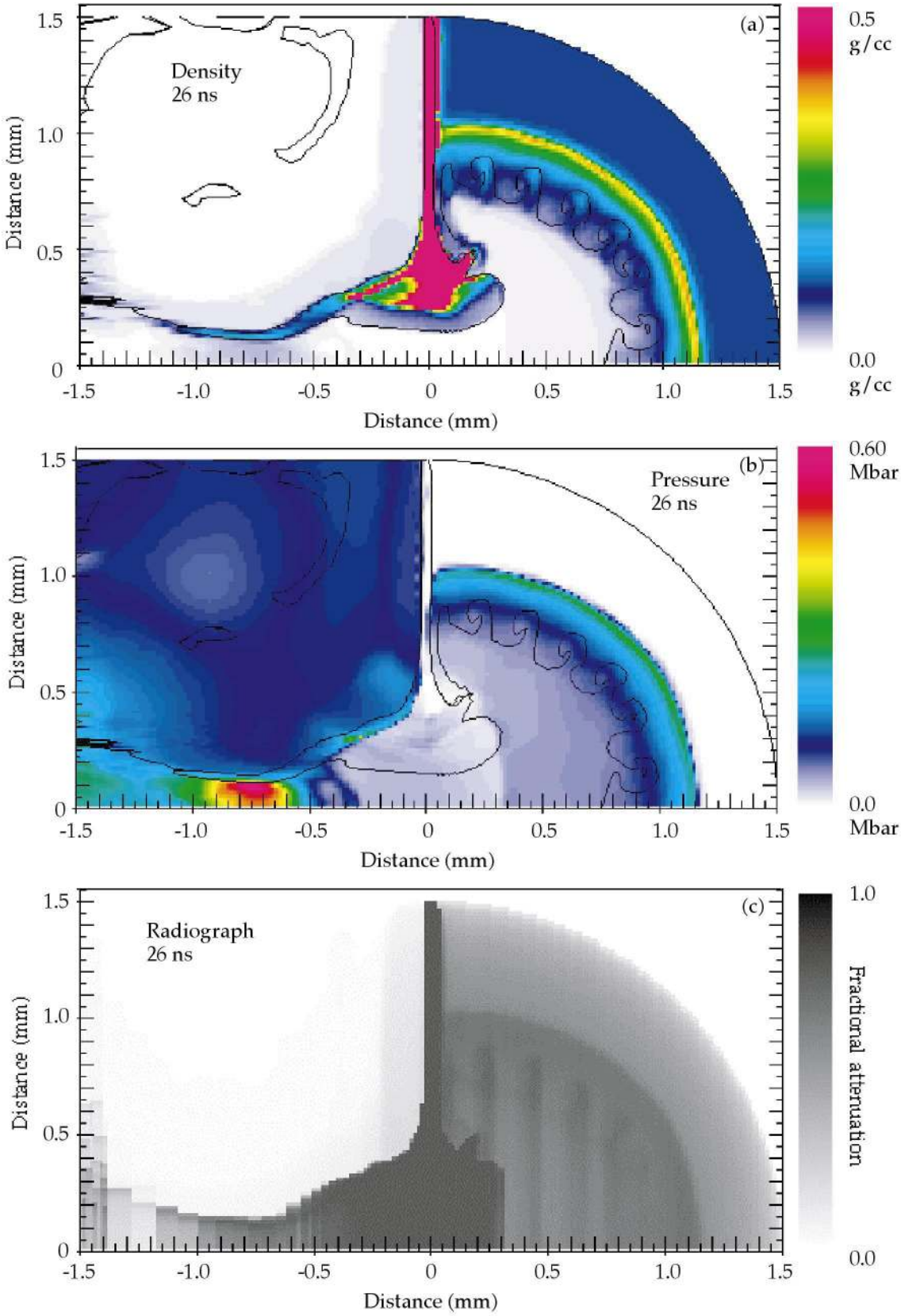

FIG. 10.—Plots of (*a*) the material density, (*b*) the pressure, and (*c*) the transmission radiograph at $t = 26$ ns. In (*a*) the color levels range from 0 to 0.5 g cm^{-3}. In (*b*) the color levels range from 0 to 0.6 Mbar (6×10^{11} dyne cm^{-3}). Material boundaries are traced with thin black lines.

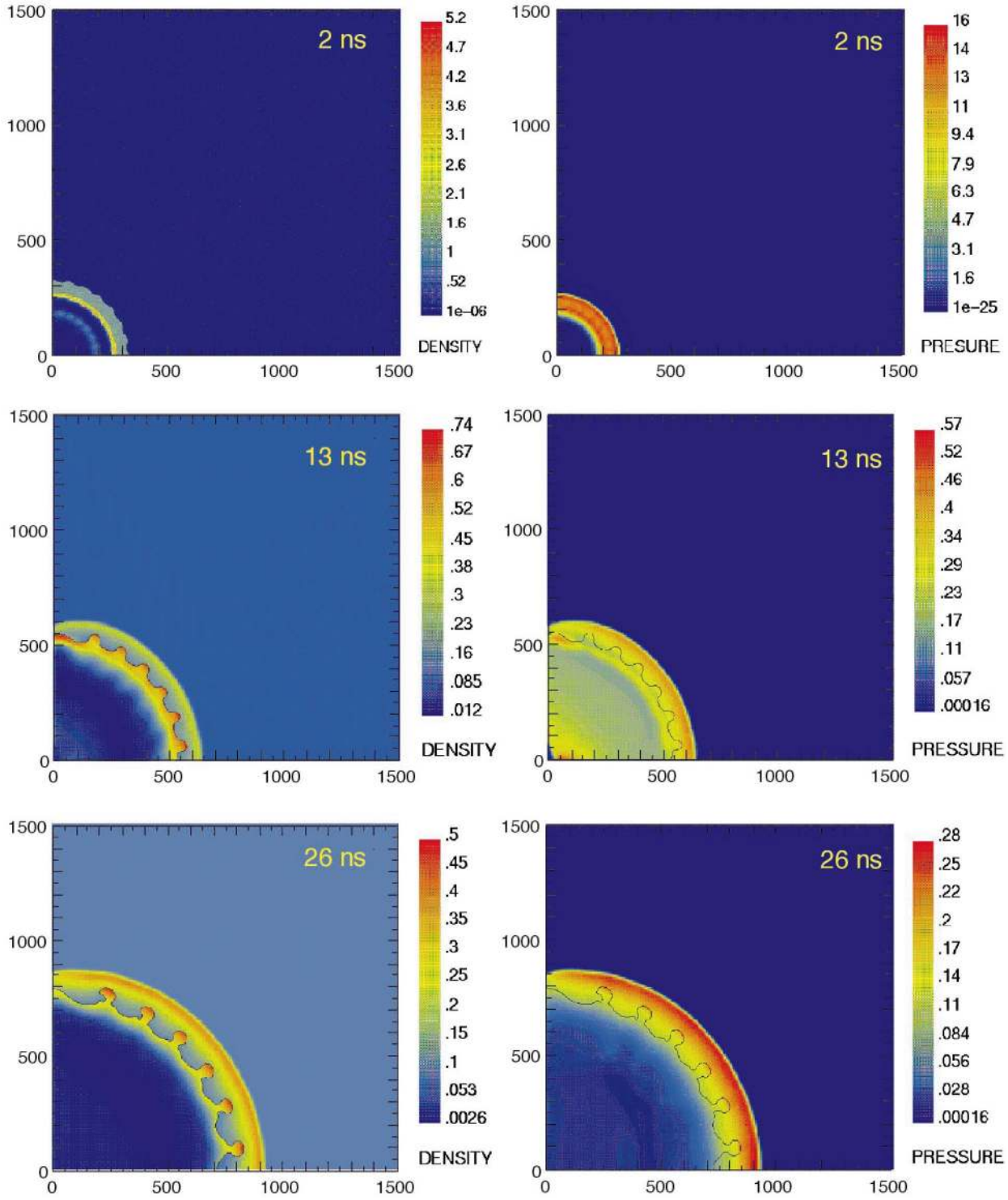

FIG. 11.—Results from the FronTier hydrodynamic code. The structure of the density and pressure are shown at times of 2, 13, and 26 ns, as labeled. The color scales show the density in g cm^{-3} and the pressure in Mbar (1 Mbar = 10^{12} dyne cm^{-2}), as labeled. All the axes give distances in μm.

use the MUSCL (monotonic upstream-centered scheme for conservation laws) algorithm to update the states along each side of the front. Finally, we update the states in the interior smooth region using the MUSCL algorithm with the front data as a boundary condition. By tracking discontinuous waves, one can explicitly include jumps in the variables across the waves and keep all discontinuities perfectly sharp. Thus, we never perform finite differencing across the front. The main advantage of the front-tracking method is that it completely eliminates the numerical diffusion that is inherent in any standard finite-difference method; thus, the front remains perfectly sharp all the time. This statement applies to mass diffusion as well as to interfacial vorticity, which is a leading contribution to numerical dissipation. In addition, the nonlinear instability and postshock oscillations common to other methods are reduced by explicitly tracking the front. This method has been proved to be very successful in wide range of interface instability simulations

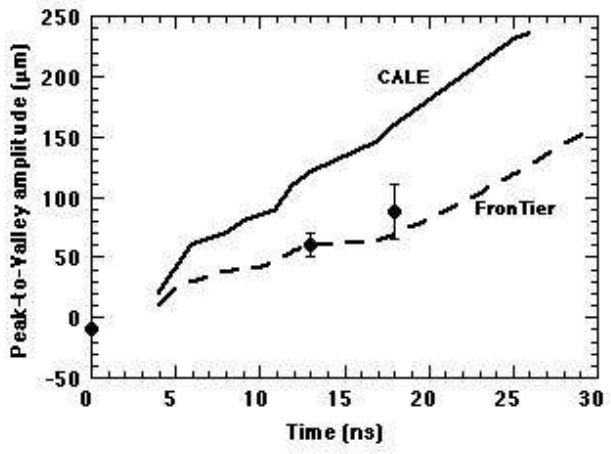

FIG. 12.—Perturbation amplitude (μm) vs. time (ns). The solid line shows the average peak-to-valley amplitude determined by tracking the material boundaries in the CALE simulation. The dashed line shows the average peak-to-valley amplitude determined by the front-tracking code FronTier, using the CALE results at 2 ns as an initial condition. The data points show the amplitudes determined, as described in the text, from the experimental radiographs.

(Chern et al. 1986; Glimm et al. 1986; Grove 1994; Zhang & Graham 1998; Glimm, Grove, & Zhang 2001). For a more detailed description of the front-tracking method, see Chern et al. (1986).

In order to apply FronTier to the present problem, we used the data produced by CALE at 2 ns, as described above. The data from CALE are interpolated onto a rectangular (r, z) grid of 200 × 200 zones. We use a 1500 μm square computational domain. The boundary conditions are implemented as follows. First, we replace the gold shield by a fixed boundary. In the open region inside the capsule, at small radii, we implement a time-dependent, outflow boundary condition as follows. In order to update the boundary state, we imagine that there exists a far-field state defined by the extrapolation of the states near the boundary point. Then we solve the Riemann problem, using the interior state near the boundary and the extrapolated far-field state, and retain only the incoming waves. This boundary is equivalent to an open boundary and an infinitely large domain. All waves will propagate out of the domain, and no boundary signal will be reflected back, at least theoretically. The flow-through boundary condition is also applied to the outer boundaries at large radius and large axial distance boundaries. A reflective boundary condition is used for the axis of rotation.

In the resulting simulation, there were two shocks present inside the capsule at 2 ns. One moved outward and hit the perturbed interface; the other moved inward to the center of the capsule. Because of the boundary condition just described, the inward shock wave exited the domain and did not bounce back from the origin. Therefore, there was no second shock through the perturbed interface. The Mach number of the forward shock is around 300. Figure 11 displays the density and pressure plots for 2 ns, 13 ns, and 26 ns. Here, the horizontal axis is the axis of rotation, as it is in the prior figures.

By comparing Figure 11 with Figures 9 and 10, one can see that CALE and FronTier produced qualitatively similar results. Quantitatively, there were some differences. By 13 ns, the inside surface of the capsule had moved to $\sim$500 μm in the FronTier results, $\sim$600 μm in the data, and $\sim$700 μm in the CALE results. The corresponding values at 26 ns were $\sim$700, $\sim$750, and $\sim$800 μm. Thus, FronTier moved the capsule somewhat more slowly than it actually did move, while CALE moved it somewhat more rapidly. One interpretation of these results is that FronTier may have missed some energy deposition that did continue after 2 ns but that CALE produced more of this than was actually present. As we said before, using a thicker capsule in future experiments would eliminate this source of difference in the code results.

The data also show the forward shock to be much closer to the spike tips than the simulations predict. One can, for example, compare Figure 5 with Figures 9 and 11. The distance from forward shock to spike tip, at 13 ns, is seen to be $\sim$30 μm in Figure 5. (The features in the grid are 62.5 μm center to center.) In contrast, this distance is about 70 μm in the results of both simulations. It is worth noting that a similar discrepancy between data (as interpreted) and simulations has also been found in studies of supernova remnants (Chevalier 1992).

Figure 12 shows the calculated evolution of the distance from the spike tip to the bubble head in both cases, and compares this to the data at the times when one can determine this distance. Because the initial Richtmyer-Meshkov response inverts the phase of the modulation, the initial amplitude is shown as negative. FrontTier reproduces the data, but as noted above, the expansion may be underdriven in that simulation. CALE, which produced an overdriven expansion, also produces much more growth than is observed. In addition, the shape of the spike tips differs between the two codes, with FronTier producing much less curling. However, this is at a level of detail where the simulations are underresolved and where the data cannot resolve the differences. In addition to the difference in drive, other possible sources of the differences between the code results include differences in the computational method, differences in the boundary conditions, especially near the capsule center, and interpolation errors in the mapping the initial conditions. Problems with such strong shocks are not trivial to calculate correctly.

7. CONCLUSION

We have reported the results of the first experiments to produce a spherically diverging, hydrodynamically unstable system that can provide a well-scaled test of computer models of supernova explosion hydrodynamics. The system involves the brief outward acceleration of a hemispherical layer of material, against a thick layer of less dense material, by a strong, laser-generated shock, followed by an extended period of deceleration. The spatial structure near the interface between the two materials is similar to that produced (according to simulations) at the H/He interface in SN 1987A. In both the experiment and the SN, the interface is hydrodynamically unstable. In the experiment, the instability is seeded by an initial perturbation at this interface.

The data show that we have succeeded in producing a (very nearly) spherically divergent experimental test bed. The spherical divergence is sufficient to increase the wavelength of the perturbation more than threefold during the experiment. (The difference in the instability evolution between this case and planar geometry will be a subject of future work.) Experimentally, we have examined two density ratios across the interface and two perturbation

geometries. We have numerically simulated these experiments with two-dimensional CALE and FronTier. The CALE model includes the detailed laser plasma and radiation physics necessary to model both the radiation-hydrodynamics of the first 2 ns of the experiment as well as the long-term, purely hydrodynamic evolution of the system. The application of astrophysical or other hydrodynamic models to this system can begin at 2 ns. We provided an example of one such application using FronTier. This establishes the foundation for the development of more realistic and more complicated systems, such as nonspherical explosions.

The present experiments and simulations could be improved in future work. Improved simulations would employ finer meshes. One could also undertake a further analysis of the differences among the simulations. An improved experiment would use a thicker capsule, to better assure that the system became purely hydrodynamic before the shock left the capsule. In addition, better images of the modulations and spike structure would be useful. To this end, future experiments could work with higher magnification and brighter backlighting, to obtain better images. Experiments that varied the energy of the backlighting X-rays would also help reveal the details of the structures. It would also be worthwhile, once the technology for manufacturing foam advances sufficiently, to produce a density gradient in the low-density foam, which would improve the similarity to the actual stellar geometry.

We acknowledge the technical support of the target fabrication personnel at the Lawrence Livermore National Laboratory, and of the Omega Laser Operations team. Both were essential to the success of this work. Financial support for this work included funding from the US Department of Energy to the University of Michigan, the University of Arizona, and the State University of New York at Stony Brook, and to the Lawrence Livermore National Laboratory under contract W-7405-ENG48.

REFERENCES

Arnett, D. 2000, in Ann. NY Acad. Sci., 898, Astrophysical Turbulence and Convection, ed. J. R. Buchler & H. Kandrup, 77
Arnett, W. D., Bahcall, J. N., Kirschner, R. P., & Woolsey, S. E. 1989, ARA&A, 27, 629
Barton, R. T. 1985, in Numerical Astrophysics, ed. J. M. Centrella (Boston: Jones & Bartlett), 482
Bazan, G., & Arnett, D. 1998, ApJ, 496, 316
———. 1994, ApJ, 433, L41
Boehly, T. R., et al. 1995, Rev. Sci. Intsrum., 66, 508
———. 1997, Opt. Commun., 133, 495
Bradley, D. K., et al. 1998, Phys. Plasmas, 5, 1870
Braginski, S. I. 1965, Reviews of Plasma Physics (New York: Consultants Bureau)
Budil, K. S., et al. 1996, Rev. Sci. Instrum., 67, 485
Chern, I. L., et al. 1986, J. Comput. Phys., 62, 83
Chevalier, R. A. 1992, Nature, 355, 691
Chevalier, R. A., Blondin, J. M., & Emmering, R. T. 1992, ApJ, 392, 118
Clerouin, J. G., Cherfi, M. H., & Zerah, G. 1998, Europhys. Lett., 42, 37
Connor, J. W., & Taylor, J. B. 1977, Nucl. Fusion, 17, 1067
Dimonte, G., & Wiley, L. G. 1991, Phys. Rev. Lett., 67, 1755
Drake, R. P. 1999, J. Geophys. Res., 104, 14
Glimm, J., Grove, J., & Zhang, Y. 2001, SIAM J. Sci. Comput., submitted
Glimm, J., et al. 1986, SIAM J. Sci. Statist. Comput., 7, 230
———. 2001, J. Comput. Phys., 169, in press
Grove, J. W. 1994, J. Appl. Num. Math., 14, 213
Grun, J., et al. 1991, Phys. Rev. Lett., 66, 2738
Hachisu, I., et al. 1991, ApJ, 368, L27
Herant, M., & Benz, W. 1991, ApJ, 370, L81
———. 1992, ApJ, 387, 294
Kane, J., et al. 1997, ApJ, 478, L75
Kane, J., et al. 1998, in Stellar Evolution, Stellar Explosions and Galactic Chemical Evolution, Second Oak Ridge Symp. on Atomic and Nuclear Astrophysics, ed. A. Mezzacappa (Philadelphia: Inst. Physics), 657
———. 1999, Phys. Plasmas, 6, 2065
———. 2000, ApJ, 528, 989
Khokhlov, A. M., et al. 1999, ApJ, 524, L107
Kifonidis, K., et al. 2000, ApJ, 531, L123
Larsen, J. T., & Lane, S. M. 1994, J. Quant. Spectrosc. Radiat. Transfer, 51, 179
Lee, Y. T., & More, R. M. 1984, Phys. Fluids, 27, 1273
Leith, C. E. 1990, Phys. Fluids A, 2, 297
Lindl, J. D. 1998, Inertial Confinement Fusion (New York, Springer)
MacLow, M.-M. 1995, Nature, 377, 287
McCray, R. 1993, ARA&A, 31, 175
Muller, E., Fryxell, B., & Arnett, D. 1991, A&A, 251, 505
Piomelli, U., Cabor, W. H., Moin, P., & Lee, S. 1991, Phys. Fluids A, 3, 1766
Remington, B. A., Arnett, D., Drake, R. P., & Takabe, H. 1999, Science, 284, 1488
Remington, B. A., Drake, R. P., Arnett, D., & Takabe, H. 2000, Phys. Plasmas, 7, 1641
Remington, B. A., et al. 1997, Phys. Plasmas, 4, 1994
Ripin, B. H., et al. 1987, Phys. Rev. Lett., 59, 2299
———. 1990, Laser Part. Beams, 8, 183
———. 1993, Phys. Fluids B, 5, 3491
Ryutov, D. D., et al. 1999, ApJ, 518, 821
Soures, J. M., et al. 1996, Phys. Plasmas, 3, 2108
Stone, J. M., Xu, J., & Mundy, L. G. 1995, Nature, 377, 315
Zhang, Q., & Graham, M. J. 1998, Phys. Fluids, 10, 974